Three-Dimensional, Flexible Nanoscale Field-Effect Transistors as Localized Bioprobes

Bozhi Tian, *et al.*

Science **329**, 830 (2010);
DOI: 10.1126/science.1192033

This copy is for your personal, non-commercial use only.

If you wish to distribute this article to others, you can order high-quality copies for your colleagues, clients, or customers by clicking here.

Permission to republish or repurpose articles or portions of articles can be obtained by following the guidelines here.

The following resources related to this article are available online at www.sciencemag.org (this information is current as of August 19, 2010):

Updated information and services, including high-resolution figures, can be found in the online version of this article at:
http://www.sciencemag.org/cgi/content/full/329/5993/830

Supporting Online Material can be found at:
http://www.sciencemag.org/cgi/content/full/329/5993/830/DC1

This article **cites 24 articles**, 8 of which can be accessed for free:
http://www.sciencemag.org/cgi/content/full/329/5993/830#otherarticles

This article appears in the following **subject collections**:
Physics, Applied
http://www.sciencemag.org/cgi/collection/app_physics

Downloaded from www.sciencemag.org on August 19, 2010

Science (print ISSN 0036-8075; online ISSN 1095-9203) is published weekly, except the last week in December, by the American Association for the Advancement of Science, 1200 New York Avenue NW, Washington, DC 20005. Copyright 2010 by the American Association for the Advancement of Science; all rights reserved. The title *Science* is a registered trademark of AAAS.

by small-scale convection. The induced relative sea-level variations are regionally correlatable and are synchronous or nearly synchronous over spatial scales that encompass the dimensions of most shelf-slope systems of sedimentary basins, where sequences are most readily identifiable. This poses a challenge for the use of sequence stratigraphy in regional and global correlation as well as in the construction of global sea-level records. If IP sequences are indeed controlled by sublithospheric convection, they can only be considered locally for dating sedimentary successions. Our study thus provides an explanation for the enigmatic control on IP cycles, between the shorter-period variations caused by Milankovich cycles and those caused by regional in-plane stress changes and other tectonic and nontectonic contributions, including glacio-eustatic sea-level variations.

References and Notes

1. O. Catuneanu *et al.*, *Earth Sci. Rev.* **92**, 1 (2009).
2. B. U. Haq, J. Hardenbol, P. R. Vail, *Science* **235**, 1156 (1987).
3. A. D. Miall, *Geology* **20**, 787 (1992).
4. N. Christie-Blick, G. S. Mountain, K. G. Miller, *Science* **241**, 596 (1988).
5. P. J. Tackley, *Nat. Geosci.* **1**, 157 (2008).
6. F. M. Richter, *J. Geophys. Res.* **78**, 8735 (1973).
7. B. Parsons, D. McKenzie, *J. Geophys. Res.* **83** (B9), 4485 (1978).
8. W. R. Buck, *Nature* **313**, 775 (1985).
9. R. Stephenson, C. Beaumont, in *Mechanisms of Continental Drift and Plate Tectonics*, P. A. Davies, K. Runcorn, Eds. (Academic Press, London, 1980), pp. 111–122.
10. M. D. Ballmer, J. van Hunen, G. Ito, P. J. Tackley, T. A. Bianco, *Geophys. Res. Lett.* **34**, L23310 (2007).
11. S. D. King, J. Ritsema, *Science* **290**, 1137 (2000).
12. G. Ranalli, *Rheology of the Earth* (Chapman & Hall, London, ed. 2, 1995).
13. See supporting data on *Science* Online.
14. S. I. Karato, P. Wu, *Science* **260**, 771 (1993).
15. S. I. Karato, *Geophys. Res. Lett.* **19**, 2255 (1992).
16. J. Huang, S. Zhong, J. Van Hunen, *J. Geophys. Res. B: Solid Earth* **108**, 2405 (2003).
17. R. Moucha *et al.*, *Earth Planet. Sci. Lett.* **271**, 101 (2008).
18. L. L. Sloss, *Geol. Soc. Am. Bull.* **74**, 93 (1963).
19. S. Spasojević, L. Liu, M. Gurnis, R. D. Müller, *Geophys. Res. Lett.* **35**, L08305 (2008).
20. R. M. Mitchum, *Am. Assoc. Pet. Geol. Mem.* **26**, 53 (1977).
21. D. McKenzie, *Earth Planet. Sci. Lett.* **40**, 25 (1978).
22. C. E. Keen, in *Continental Extensional Tectonics* (Blackwell Scientific, London, 1987), p. 67.
23. W. R. Buck, *Earth Planet. Sci. Lett.* **77**, 362 (1986).
24. K. G. Miller *et al.*, *Science* **310**, 1293 (2005).
25. A. D. Miall, *The Geology of Stratigraphic Sequences* (Springer, Berlin, 1997).
26. S. Cloetingh, H. McQueen, K. Lambeck, *Earth Planet. Sci. Lett.* **75**, 157 (1985).
27. S. B. Nielsen, E. Thomsen, D. L. Hansen, O. R. Clausen, *Nature* **435**, 195 (2005).
28. R. D. Müller, M. Sdrolias, C. Gaina, B. Steinberger, C. Heine, *Science* **319**, 1357 (2008).
29. A. Embry, Search and Discovery, www.searchanddiscovery.com/documents/2009/30105embry/ (2009).

30. We thank M. Huuse, E. Thomsen, N. Christie-Blick, and three anonymous reviewers for constructive suggestions and D. L. Egholm for providing computational facilities.

Supporting Online Material

www.sciencemag.org/cgi/content/full/329/5993/827/DC1
Methods
Figs. S1 to S7
Table S1
References
Movie S1

26 March 2010; accepted 2 July 2010
10.1126/science.1190115

Three-Dimensional, Flexible Nanoscale Field-Effect Transistors as Localized Bioprobes

Bozhi Tian,[1]* Tzahi Cohen-Karni,[2]* Quan Qing,[1] Xiaojie Duan,[1] Ping Xie,[1] Charles M. Lieber[1,2]†

Nanoelectronic devices offer substantial potential for interrogating biological systems, although nearly all work has focused on planar device designs. We have overcome this limitation through synthetic integration of a nanoscale field-effect transistor (nanoFET) device at the tip of an acute-angle kinked silicon nanowire, where nanoscale connections are made by the arms of the kinked nanostructure, and remote multilayer interconnects allow three-dimensional (3D) probe presentation. The acute-angle probe geometry was designed and synthesized by controlling cis versus trans crystal conformations between adjacent kinks, and the nanoFET was localized through modulation doping. 3D nanoFET probes exhibited conductance and sensitivity in aqueous solution, independent of large mechanical deflections, and demonstrated high pH sensitivity. Additionally, 3D nanoprobes modified with phospholipid bilayers can enter single cells to allow robust recording of intracellular potentials.

Nanowire and nanotube electrical devices have been exploited for ultrasensitive detection of biological markers (*1*) and high-resolution extracellular recording from cells (*2*–*5*). However, localized and tunable three-dimensional (3D) sensing and recording with the prototypical nanoelectronic device, a nanoscale field-effect transistor (nanoFET) (*6*), have not been demonstrated because almost all examples of these devices are created on planar substrates. Ideally, rather than force the cell to conform to the substrate, a movable nanoFET with the necessary source (S) and drain (D) electrical connections could move into contact with the cell and probe within the cell membrane. However, minimally invasive insertion of a nanoFET into the confined 3D space of single cells, or even 3D cellular networks, is a major challenge because the S and D typically dominate the overall device size and define a planar and rigid structure, regardless of whether the nanoFET is on or suspended above a substrate (*5*, *6*).

Existing probes capable of intracellular sensing and recording include voltage-sensitive optical dyes (*7*, *8*) and single-terminal glass (*9*–*11*) or carbon (*12*–*14*) microelectrodes. Voltage-sensitive dyes can readily be used to interrogate action potentials with high spatial resolution, but they also have limitations in terms of signal-to-noise (S/N) ratio, pharmacological side effects, phototoxicity, and difficulty in differentiating single spikes (*7*, *8*). For electrical probes, the single electrical connection facilitates design and mechanical insertion into cells, but the requirement of direct ionic and/or electrical junctions between probe tips and cytosol also introduce several limitations. First, the tip size of these probes (~0.2 to 5 μm) (*9*–*14*) is a compromise between being small enough to penetrate or rupture the cell membrane with minimum damage (<5 μm) and large enough to yield a junction impedance that is sufficiently low (>0.2 μm) (*9*, *11*) so that small cellular signals can be discerned from thermal noise. Second, direct exposure of intracellular species to extraneous probe surfaces or electrolytes in probe lumen (*9*–*13*), especially for larger glass micropipettes, might induce irreversible changes to cells and, thus, prevent long-term and noninvasive cellular recordings. Finally, these probe techniques are intrinsically passive and are not capable of built-in signal processing and facile integration with other circuitries, especially given the emerging need to enable a cell-machine communication (*15*).

FETs can function in a sub–10-nm-size regime (*16*). NanoFETs could function as mechanically noninvasive probes capable of entering cells through endocytic pathways, as can occur with nanoparticles (*17*). Moreover, when interfacing with cells, the FETs process input/output information without the need for direct exchange with cellular ions; thus, interfacial impedance and biochemical invasiveness to cells can be minimized. In addition, because signals are transduced by change in field/potential at well-isolated surfaces, FETs can detect cellular potential (*2*–*5*), as well as biological macromolecules (*1*), and could be integrated for potential multiplexed intracellular measurements. Unfortunately, and as discussed above, the requirement of two electrical contacts to a FET, the S and D, makes design of 3D probes

---

[1]Department of Chemistry and Chemical Biology, Harvard University, Cambridge, MA 02138, USA. [2]School of Engineering and Applied Sciences, Harvard University, Cambridge, MA 02138, USA.

*These authors contributed equally to this work.

†To whom correspondence should be addressed. E-mail: cml@cmliris.harvard.edu

and their minimally invasive insertion into a cell or tissue a substantial challenge.

Recently, we demonstrated that variation of reactant pressure during silicon nanowire (SiNW) growth could introduce reproducible 120° kinks (*18*) and that the junction regions could be doped to create p-n diodes and FETs. We used this methodology to create a two-terminal FET probe that could be inserted into single cells. The growth of kinked SiNWs had to be tailored in the following ways: First, we needed to incorporate two or three cis-linked kinked units to yield probe-tip angles of 60° or 0°, respectively (Fig. 1A, top and middle). Because two trans-linked units (Fig. 1A, bottom) would yield an unusable probe tip, the selective synthesis of cis-linked units is central to our probe-geometry design. A representative scanning electron microscopy (SEM) image of an 80-nm diameter, doubly kinked SiNW with an intervening segment length (*L*) of ~160 nm between kink units (Fig. 1B) shows well-defined cis-linkage and an overall 60° tip angle (Fig. 1A, top). To investigate our ability to synthesize this cis-linkage of kink structural units reproducibly, we analyzed their fraction as a function of *L* in doubly kinked SiNWs. Notably, the plot of cis/(cis + trans), as *L* was varied from ~700 to 50 nm (Fig. 1C), shows that the cis conformation becomes dominant as *L* decreases. We can selectively synthesize cis-linked kinked units in good yield [fig. S1A (*19*)], e.g., ~66% where *L* ~ 50 nm, and such conformation control is also maintained in the growth of complex probe structures [fig. S1B (*19*)].

The second design consideration made use of selective in situ doping during synthesis to localize and self-label the nanoscale FET element adjacent to the topologically defined probe tip (Fig. 1A, pink segments) and to simultaneously “wire-up” the FET channel with nanowire S/D components (Fig. 1A, blue segments). As in our studies of single-kinked nanowires (*18*), we used heavy n^{++}-type doping for the nanowire S/D arms and reduced the concentration to light n-type doping to introduce a short ~200-nm region immediately following the growth of two sequential kinks and serving as the “pointlike” FET

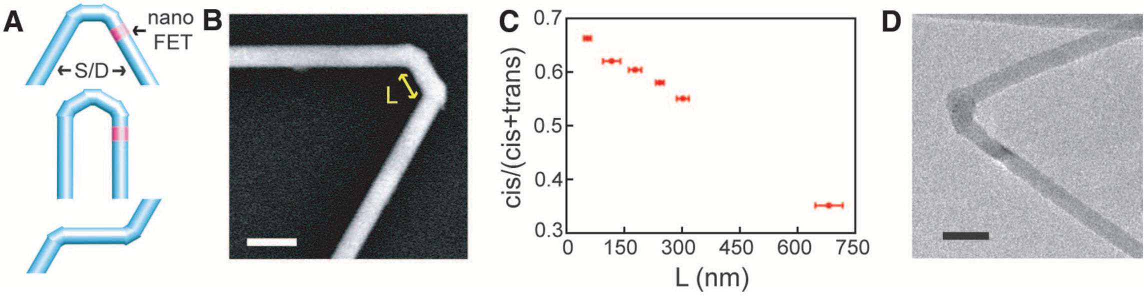

Fig. 1. Synthesis of kinked SiNW probes. (**A**) Schematics of 60° (top) and 0° (middle) multiply kinked nanowires and cis (top) and trans (bottom) configurations in nanowire structures. The blue and pink regions designate the source/drain (S/D) and nanoscale FET channel, respectively. (**B**) SEM image of a doubly kinked nanowire with a cis configuration. *L* is the length of segment between two adjacent kinks. (**C**) cis/(cis + trans) versus *L* plot. Error bars indicate ±1 SD from the mean. (**D**) Transmission electron microscopy image of an ultrathin 60° kinked nanowire. Scale bars, 200 nm (B); 50 nm (D).

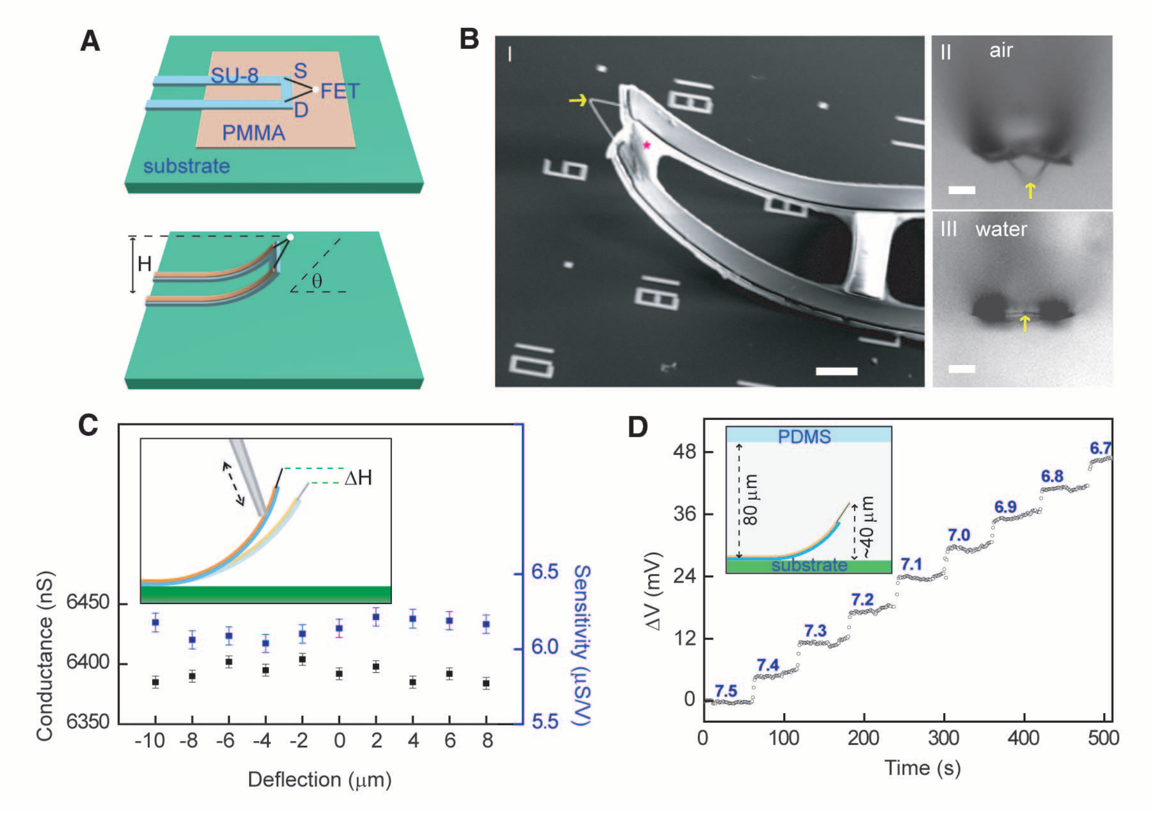

Fig. 2. 3D kinked nanowire probes. (**A**) Schematics of device fabrication. Patterned poly(methyl methacrylate) and SU-8 microribbons [see supporting online material (SOM) materials and methods (*19*)] serve as a sacrificial layer and flexible device support, respectively. The dimensions of the lightly doped n-type silicon segment (white dots) are ~80 by 80 by 200 nm^3. *H* and θ are the tip height and orientation, respectively, and S and D designate the built-in source and drain connections to the nanoscale FET. (**B**) SEM (I) and bright-field optical microscopy (II, III) images of an as-made device. The yellow arrow and pink star mark the nanoscale FET and SU-8, respectively. II and III are recorded in air and water, respectively. Scale bars, 5 μm. (**C**) Device conductance and sensitivity as a function of deflection of the probe using a micropipette controlled with a micromanipulator. The measurements were carried out in PBS solution. Error bars indicate ±1 SD from the mean. (Inset) Experimental scheme. Δ*H*, change in tip height. (**D**) Change in potential versus solution pH for a representative 3D nanowire probe. (Inset) Experimental scheme. For clarity, the pointlike FET elements are not labeled in the schematics in (C) and (D).

detector of the overall probe. Scanning gate microscopy (SGM) measurements [fig. S1 (*19*)] showed that nanoscale FETs were integrated at the probe tip during overall synthesis.

We have also examined the size limits of these synthetic bioprobes in terms of the overall nanowire diameter and length *L* between kinks, and we found that well-defined probe structures are possible for values as small as ~18 and 15 nm, respectively (Fig. 1D and fig. S2) (*19*). These data show that it is possible to create active semiconductor probes with dimensions smaller than microtubules in cells (*20*).

We next designed an unconventional nanoelectronic-device–fabrication approach that would allow these probes to be used as cellular probes. We made remote electrical interconnects to the S/D nanowire arms on ultrathin SU-8 polymer ribbons above a sacrificial layer (Fig. 2A, top). The interfacial stress between materials (*21*) was used to bend the probe upward after a final lift-off process (Fig. 2A, bottom); see fig. S3A for fabrication details (*19*). Our nanoprobes are distinct from previous nanoelectronic devices because (i) the FET channel (Fig. 2A, white dots) and S/D (Fig. 2A, black segments) components are integrated epitaxially at the nanoscale through synthesis (Fig. 1), similar to single-kink structures (*18*), (ii) the nanoscale FET is free-standing, and (iii) the acute-angle kinked-nanowire geometry and extended S/D arms spatially separate the functional nanoscale FET from the bulky interconnects by a distance up to ~30 µm, comparable to the size of single cells, so that the nanoscale interrogation can be realized with minimum interference from macroscopic interconnects.

A representative SEM image of one free-standing device (Fig. 2B, I) demonstrates that the 60° kinked probe is intact after fabrication with the two nanowire arm terminals sandwiched between the SU-8 polymer and the metal contacts. We achieved ≥90% yields with ~30 nanoprobe devices per chip. In addition, the probe height and angle (H and θ, Fig. 2A) were systematically tuned by changing the length and thickness of the free-standing part of the metal interconnects/SU-8 backbone (fig. S3B) (*19*). We also found that the nanoprobe H and θ typically increase when submerged in aqueous solution [H/θ of the device (Fig. 2B, I) are 25 µm/43° and 38 µm/90° in air and water, respectively (Fig. 2B, II and III)]. This change is reversible and suggests that the nanoprobe devices are intrinsically flexible, and moreover, that the specific orientation could be manipulated chemically (*21*). Last, free-standing 3D FET devices have been stored in air for at least 8 months without appreciable changes in nanoprobe orientations and FET sensitivity (<7 and 3%, respectively).

The sensitivity of the 3D nanoscale FET probes was characterized in phosphate-buffered saline (PBS) solution (Fig. 2C and fig. S4A). Measurements of the conductance versus reference potential for the 3D probes yielded sensitivities of 4 to 8 µS/V. Similar sensitivities, 4 to 8 µS/V, were observed for kinked nanowire devices fabricated on planar substrates, thus indicating that there is no degradation in the bent 3D configuration. We note that the sensitivity contribution from the lightly doped nanoFET is >97% of the total device response. Localized detection by the lightly doped region versus the heavily doped S/D nanowire arms is consistent with our SGM measurements on these acute-angle probes (fig. S1) and previous studies of single-kinked nanowires (*18*).

To further highlight the flexibility and robustness of the 3D nanoFET probes, we have characterized the conductance and sensitivity in PBS as a glass micropipette was used to vary the tip height (Fig. 2C, inset). Typical data (Fig. 2C) yield a <20-nS conductance change for a ~±10-µm change in H, which corresponds to <0.31% fluctuation in the total device conductance. Likewise, the device sensitivity remains stable with a maximum change of ~0.15 µS/V or 2.4% variation for this ~±10-µm tip-height change. In addition, repetitive bending does not degrade

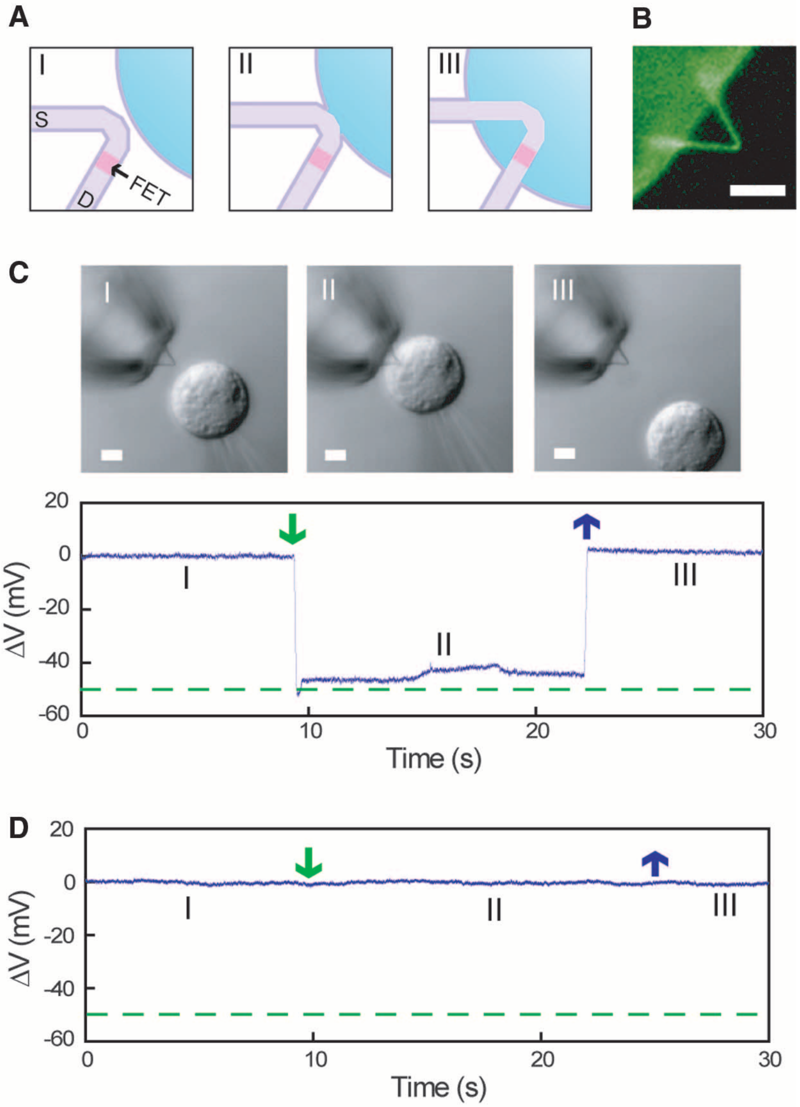

Fig. 3. Surface modification and cellular entry. (**A**) Schematics of nanowire probe entrance into a cell. Dark purple, light purple, pink, and blue colors denote the phospholipid bilayers, heavily doped nanowire segments, active sensor segment, and cytosol, respectively. (**B**) False-color fluorescence image of a lipid-coated nanowire probe. DMPC was doped with 1% nitrobenzoxadiazole dye–labeled lipids and imaged through a 510/21 band-pass filter. (**C**) Differential interference contrast microscopy images (upper panels) and electrical recording (lower panel) of an HL-1 cell and 60° kinked nanowire probe as the cell approaches (I), contacts and internalizes (II), and is retracted from (III) the nanoprobe. A pulled-glass micropipette (inner tip diameter ~ 5 µm) was used to manipulate and voltage clamp the HL-1 cell. The dashed green line corresponds to the micropipette potential. Scale bars, 5 µm. (**D**) Electrical recording with a 60° kinked nanowire probe without phospholipids surface modification. Green and blue arrows in (C) and (D) mark the beginnings of cell penetration and withdrawal, respectively.

the FET performance in these nanowire probes. Finally, the stable FET performance in different bending configurations suggests the capability of reliable sensing and recording in a flexible and tunable 3D manner from single devices, which could be particularly beneficial for interfacing with soft and motile biological systems.

We tested the sensing capabilities of the 3D SiNW probes by recording the response to variations in solution pH within a polydimethylsiloxane (PDMS) microfluidic channel (Fig. 2D, inset). Stepwise potential increases from 7.5 to 6.7 by 0.1 pH units were readily resolved, and the sensitivity of ~58 mV/pH was near the Nernstian limit. High-resolution recording indicates the capability of resolving changes as small as 0.02 pH units [fig. S4B (*19*)] in this physiologically relevant range of pH.

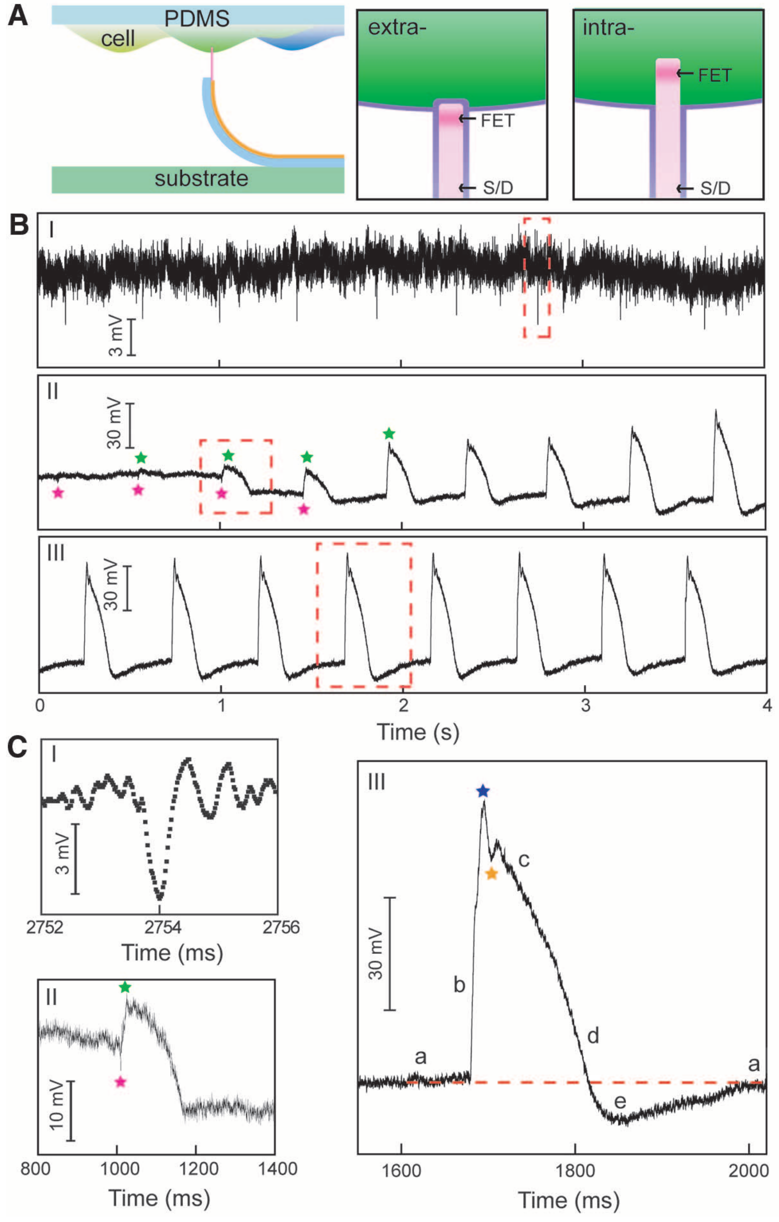

Fig. 4. Electrical recording from beating cardiomyocytes. (**A**) Schematics of cellular recording from the cardiomyocyte monolayer on PDMS (left) and highlight of extracellular (middle) and intracellular (right) nanowire/cell interfaces. The cell membrane and nanowire lipid coatings are marked with purple lines. (**B**) Electrical recording from beating cardiomyocytes: (i) extracellular recording, (ii) transition from extracellular to intracellular recordings during cellular entrance, and (iii) steady-state intracellular recording. Green and pink stars denote the peak positions of intracellular and extracellular signal components, respectively. The red-dashed boxes indicate regions selected for (C). (**C**) Zoom-in signals from the corresponding red-dashed square regions in (B). Blue and orange stars designate features that are possibly associated with inward sodium and outward potassium currents, respectively. The letters a to e denote five characteristic phases of a cardiac intracellular potential, as defined in text. The red-dashed line is the baseline corresponding to intracellular resting state. The cell culture, electronics, and recording details are specified in the SOM materials and methods section (*19*).

To use the 3D nanoFET probes in cells (Fig. 3A), we coated them with phospholipid bilayers, which can form on a variety of nanostructured inorganic materials (*22*–*24*) and also fuse with cell membranes (*24*). Accordingly, we modified the negatively charged SiO_2 surface of the SiNWs by fusion with unilamellar vesicles of phospholipid bilayers [1,2-dimyristoyl-sn-glycero-3-phosphocholine (DMPC)] (*19*, *22*). Fluorescence microscopy images of dye-labeled DMPC modified probes (Fig. 3B) indicate that the lipid bilayers form a continuous shell on our acute-angle nanoprobes, and device measurements show that the lipid surface coating results in <1% changes in both the nanoFET conductance and sensitivity. We then monitored the calibrated potential change of phospholipid-modified nanoFET probe while an isolated HL-1 cell (*25*) was moved into contact and then away from the nanoprobe using a glass micropipette under microscopy visualization (Fig. 3C, top). The micropipette was also used to clamp the intracellular potential at –50 mV (*11*). Notably, measurement of the potential versus time from the nanoFET probe shows a sharp ~52-mV drop within 250 ms after cell-to-tip contact. While the nanoprobe tip is within the cell, the recorded potential maintains a relatively constant value of ~–46 mV and then returns to baseline when the cell was detached from the nanowire probe end. NanoFET probes of similar sensitivity that were not coated with a phospholipid bilayer modification exhibited only baseline fluctuations (<±1 mV), as the HL-1 cell was brought into contact and then retracted (Fig. 3D). These results suggest that the biochemical state of the nanowire probe surfaces (*26*) is critical for assisting access to the intracellular region, possibly through membrane fusion (Fig. 3A) (*24*), and is distinct from larger, more rigid probes commonly used for intracellular electrical recording.

We have also investigated the formation of intracellular interfaces between our 3D nanoFET probes and spontaneously firing electrogenic cells. Embryonic chicken cardiomyocytes were cultured on PDMS substrates (*2*) and then positioned to place individual cells over phospholipid bilayer–modified vertical (θ = 90°) nanoprobes within a cell-perfusion chamber (*2*, *4*), as shown schematically in Fig. 4A. Representative conductance-versus-time data recorded from a 3D nanoFET probe initially in gentle contact with a spontaneously beating cardiomyocyte cell (fig. S5A) (*19*) showed a sequence of distinct features (Fig. 4B). Initially, we observed regularly spaced spikes with a frequency of ~2.3 Hz, consistent with the beating cardiomyocyte (Fig. 4B, I). The peaks have a potential change of ~3 to 5 mV, a S/N ratio ≥ 2, and a submillisecond width (Fig. 4C, I). The peak amplitude, shape, and width are similar to extracellular recordings made with nanowire devices on substrates (*2*); moreover, optical images recorded at the same time [fig. S5A (*19*)] are consistent with extracellular signals.

After a relatively brief (~40-s) period of extracellular signals, we observed several pronounced changes in recorded signals (Fig. 4, B and C, II and III) without application of external force to the PDMS/cell support. Specifically, the initial extracellular signals gradually disappeared (Fig. 4, B and C, II, pink stars). There was a concomitant decrease in baseline potential, and new peaks emerged that had an opposite sign, similar frequency, much greater amplitude, and longer duration (Fig. 4B, II, green stars). These new peaks, which are coincident with cardiomyocyte cell beating, rapidly reached a steady state (Fig. 4B, III) with an average calibrated peak amplitude of ~80 mV and duration of ~200 ms. The amplitude, sign, and duration are near those reported for whole-cell patch clamp recordings from cardiomyocytes (*27*, *28*); thus, we conclude that these data represent a transition to steady-state intracellular recording (Fig. 4A, right) with the 3D nanowire probe.

Detailed analysis of the latter steady-state peaks (Fig. 4C, III) shows five characteristic phases of a cardiac intracellular potential (*27*, *28*), including (a) resting state, (b) rapid depolarization, (c) plateau, (d) rapid repolarization, and (e) hyperpolarization. In addition, a sharp transient peak (blue star) and the notch (orange star) possibly associated with the inward sodium and outward potassium currents (*28*) can be resolved. Optical images recorded at the same time as these intracellular peaks (fig. S5B) showed the kinked nanowire probe tips in a possible intracellular region of the cell (*19*). When the PDMS/cell substrate was mechanically retracted from the 3D kinked nanowire devices, the intracellular peaks disappeared, but they reappeared when the cell substrate was brought back into gentle contact with the device. This process could be repeated multiple times without degradation in the recorded signal. When vertical 3D nanoprobe devices were bent into a configuration with angle θ < ~50° with respect to the substrate, or when kinked nanowire devices were fabricated on planar substrates, we could record only extracellular signals. These results confirm that electrical recording arises from the highly localized, pointlike nanoFET near the probe tip, which (i) initially records only extracellular potential, (ii) simultaneously records both extracellular and intracellular signals as the nanoFET spans the cell membrane, and (iii) records only intracellular signals when fully inside the cell.

Additional work remains to develop this new synthetic nanoprobe as a routine tool like the patch-clamp micropipette (*10*, *11*), although we believe that there are already clear advantages: Electrical recording with kinked nanowire probes is relatively simple without the need for resistance or capacitance compensation (*9*, *11*); the nanoprobes are chemically less invasive than pipettes, as there is no solution exchange; the small size and biomimetic coating minimizes mechanical invasiveness; and the nanoFETs have high spatial and temporal resolution for recording.

References and Notes

1. D. A. Giljohann, C. A. Mirkin, *Nature* **462**, 461 (2009).
2. T. Cohen-Karni, B. P. Timko, L. E. Weiss, C. M. Lieber, *Proc. Natl. Acad. Sci. U.S.A.* **106**, 7309 (2009).
3. J. F. Eschermann *et al.*, *Appl. Phys. Lett.* **95**, 083703 (2009).
4. Q. Qing *et al.*, *Proc. Natl. Acad. Sci. U.S.A.* **107**, 1882 (2010).
5. I. Heller, W. T. T. Smaal, S. G. Lemay, C. Dekker, *Small* **5**, 2528 (2009).
6. W. Lu, C. M. Lieber, *Nat. Mater.* **6**, 841 (2007).
7. A. Grinvald, R. Hildesheim, *Nat. Rev. Neurosci.* **5**, 874 (2004).
8. M. Scanziani, M. Häusser, *Nature* **461**, 930 (2009).
9. R. D. Purves, *Microelectrode Methods for Intracellular Recording and Ionophoresis* (Academic Press, London, 1981).
10. B. Sakmann, E. Neher, *Annu. Rev. Physiol.* **46**, 455 (1984).
11. A. Molleman, *Patch Clamping: An Introductory Guide to Patch Clamp Electrophysiology* (Wiley, Chichester, UK, 2003).
12. R. M. Wightman, *Science* **311**, 1570 (2006).
13. A. G. Ewing, T. G. Strein, Y. Y. Lau, *Acc. Chem. Res.* **25**, 440 (1992).
14. M. G. Schrlau, N. J. Dun, H. H. Bau, *ACS Nano* **3**, 563 (2009).
15. J. P. Donoghue, *Nat. Neurosci.* **5** (suppl.), 1085 (2002).
16. M. Ieong, B. Doris, J. Kedzierski, K. Rim, M. Yang, *Science* **306**, 2057 (2004).
17. M. Ferrari, *Nat. Rev. Cancer* **5**, 161 (2005).
18. B. Z. Tian, P. Xie, T. J. Kempa, D. C. Bell, C. M. Lieber, *Nat. Nanotechnol.* **4**, 824 (2009).
19. Materials and methods are available as supporting material on *Science* Online.
20. C. Conde, A. Cáceres, *Nat. Rev. Neurosci.* **10**, 319 (2009).
21. T. G. Leong *et al.*, *Proc. Natl. Acad. Sci. U.S.A.* **106**, 703 (2009).
22. N. Misra *et al.*, *Proc. Natl. Acad. Sci. U.S.A.* **106**, 13780 (2009).
23. X. J. Zhou, J. M. Moran-Mirabal, H. G. Craighead, P. L. McEuen, *Nat. Nanotechnol.* **2**, 185 (2007).
24. L. V. Chernomordik, M. M. Kozlov, *Nat. Struct. Mol. Biol.* **15**, 675 (2008).
25. W. C. Claycomb *et al.*, *Proc. Natl. Acad. Sci. U.S.A.* **95**, 2979 (1998).
26. B. D. Almquist, N. A. Melosh, *Proc. Natl. Acad. Sci. U.S.A.* **107**, 5815 (2010).
27. D. M. Bers, *Nature* **415**, 198 (2002).
28. D. P. Zipes, J. Jalife, *Cardiac Electrophysiology: From Cell to Bedside* (Saunders, Philadelphia, ed. 2, 2009).

29. We thank G. Yellen, W. C. Claycomb, B. P. Bean, P. T. Ellinor, G. H. Yu, D. Casanova, B. P. Timko, and T. Dvir for help with experiments and data analysis. C.M.L. acknowledges support from a NIH Director's Pioneer Award (5DP1OD003900), a National Security Science and Engineering Faculty Fellow (NSSEFF) award (N00244-09-1-0078), and the McKnight Foundation Neuroscience award.

Supporting Online Material

www.sciencemag.org/cgi/content/full/329/5993/830/DC1
Materials and Methods
Figs. S1 to S5
References

10 May 2010; accepted 7 July 2010
10.1126/science.1192033

Terrestrial Gross Carbon Dioxide Uptake: Global Distribution and Covariation with Climate

Christian Beer,[1]* Markus Reichstein,[1] Enrico Tomelleri,[1] Philippe Ciais,[2] Martin Jung,[1] Nuno Carvalhais,[1,3] Christian Rödenbeck,[4] M. Altaf Arain,[5] Dennis Baldocchi,[6] Gordon B. Bonan,[7] Alberte Bondeau,[8] Alessandro Cescatti,[9] Gitta Lasslop,[1] Anders Lindroth,[10] Mark Lomas,[11] Sebastiaan Luyssaert,[12] Hank Margolis,[13] Keith W. Oleson,[7] Olivier Roupsard,[14,15] Elmar Veenendaal,[16] Nicolas Viovy,[2] Christopher Williams,[17] F. Ian Woodward,[11] Dario Papale[18]

Terrestrial gross primary production (GPP) is the largest global CO_2 flux driving several ecosystem functions. We provide an observation-based estimate of this flux at 123 ± 8 petagrams of carbon per year (Pg C year^{-1}) using eddy covariance flux data and various diagnostic models. Tropical forests and savannahs account for 60%. GPP over 40% of the vegetated land is associated with precipitation. State-of-the-art process-oriented biosphere models used for climate predictions exhibit a large between-model variation of GPP's latitudinal patterns and show higher spatial correlations between GPP and precipitation, suggesting the existence of missing processes or feedback mechanisms which attenuate the vegetation response to climate. Our estimates of spatially distributed GPP and its covariation with climate can help improve coupled climate–carbon cycle process models.

Terrestrial plants fix carbon dioxide (CO_2) as organic compounds through photosynthesis, a carbon (C) flux also known at the ecosystem level as gross primary production (GPP). Terrestrial GPP is the largest global carbon flux, and it drives several ecosystem functions, such as respiration and growth. GPP thus contributes to human welfare because it is the basis for food, fiber, and wood production. In addition, GPP, along with respiration, is one of the major processes controlling land-atmosphere CO_2 exchange, providing the capacity of terrestrial ecosystems to partly offset anthropogenic CO_2 emissions.

Although photosynthesis at the leaf and canopy level are quite well understood, only tentative observation-based estimates of global terrestrial GPP have been possible so far. Plant- and stand-level GPP has previously been calculated as two times biomass production (*1*, *2*), with substantial